Electron Delocalization in Spectroelectrochemically and Computationally Characterized [Pt{(*p*-BrC_6F_4)NCH=C(Cl)NEt_2}Cl(py)]$^+$ formed by Electrochemical Oxidation of [Pt^{II} {(*p*-BrC_6F_4)NCH=C(Cl)NEt_2}Cl(py)]

Ruchika Ojha[1], John F. Boas[2], Stephen P. Best[3], Allan J. Canty[4], Peter C. Junk[5] Glen B. Deacon[1]*, Alan M. Bond[1]**

[1]School of Chemistry, Monash University, Clayton 3800 VIC, Australia, [2]School of Physics, Monash University, Clayton 3800 VIC, Australia, [3]School of Chemistry, The University of Melbourne, VIC 3010, Australia, School of Natural Sciences – Chemistry, University of Tasmania, TAS 7001, Australia. [5]College of Science & Engineering, James Cook University, Townsville, Qld, 4811, Australia,

E-mail:

Alan Bond alan.bond@monash.edu

Glen Deacon glen.deacon@monash.edu

Peter Junk peter.junk@jcu.edu.au

Abstract

[Pt{(*p*-BrC_6F_4)NCH=C(Cl)NEt_2}Cl(py)] **(1Cl)** is the product of the hydrogen peroxide oxidation of the Pt^{II} anticancer agent ([Pt{(*p*-BrC_6F_4)$NCH_2CH_2NEt_2$}Cl(py)] (**1**). Insights into electron delocalization and bonding in [Pt{(*p*-BrC_6F_4)NCH=C(Cl)NEt_2}Cl(py)]$^+$ (**1Cl$^+$**) obtained by electrochemical oxidation of **1Cl** have been gained by spectroscopic and computational studies. The **1Cl/1Cl$^+$** process is chemically and electrochemically reversible on the short timescale of voltammetry in dichloromethane (0.10 M[Bu_4N][PF_6]). Substantial stability is retained on longer timescales enabling a high yield of **1Cl$^+$** to be generated by bulk electrolysis. *In situ* IR and Visible spectroelectrochemical studies on the oxidation of **1Cl** to **1Cl$^+$** and the reduction of **1Cl$^+$** back to **1Cl** confirm the long-term chemical reversibility. DFT calculations indicate only a minor contribution to the electron density (13%) resides on the Pt metal center in **1Cl$^+$**, indicating that the **1Cl/1Cl$^+$** oxidation process is extensively ligand-based. Published X-ray crystallographic data show **1Cl** is present in only one structural form, while NMR data on the dissolved crystals revealed the presence of two closely related structural forms in an almost equimolar ratio. Solution phase EPR spectra of **1Cl$^+$** are consistent with two closely related structural forms in a ratio of about 90:10. The average g value for the frozen solution spectra (2.056 for the major species) is significantly greater than the 2.0023 expected for a free radical. Crystal Field Analysis of the EPR spectra leads to an estimate of the *5d(z^2)* character of around 6% to 10% in **1Cl$^+$**. Analysis of X-ray absorption fine structure derived from **1Cl$^+$** also supports the presence of a delocalized singly occupied metal molecular orbital with a spin density of approximately 17% on Pt. Accordingly, the considerably larger electron density distribution on the ligand framework (diminished Pt^{III} character) is proposed to contribute to the increased stability of **1Cl$^+$** compared to **1$^+$**.

Introduction

Platinum coordination complexes have played a prominent role in cancer treatment for decades.[1-3] The success of cisplatin[4-6] and the need to find solutions for severe side effects in the use of this and other Pt^{II} anticancer agents,[7, 8] have encouraged extensive research into the development of new Pt^{II} drugs and Pt^{IV} prodrugs,[9-12] as well as detailed investigations of their intracellular mechanism of action[13-15] and strategies for drug delivery.[16] Primarily, platinum complexes in their common oxidation states of II and IV have been assessed as anticancer

agents. Until recently, mononuclear Pt^{III} complexes were rarely proposed as anticancer drugs, due to the reactive nature of the unpaired electron present in the "sterically exposed d_z^2 orbitals".[17] However, the Pt^{III} oxidation state can be stabilized by using bulky ligands,[18] and now Pt^{III} complexes (monomers and dimers) are starting to attract attention for their biological activity.[19-23] For example, a Pt^{III} dimer, $[Pt_2(Spy)_4Cl_2]$ (Spy = deprotonated 2-mercaptopyridine) is active against HeLa and U937 tumor lines [19, 20] as well as CH1 and cisplatin-resistant CH1 cisR cells.[22] The Pt^{III} monomers with distorted octahedral geometry, *cis*-$[Pt^{III}(NH_3)_2(Hp_{-3H})(H_2O)_2]\cdot H_2O$ and $Pt^{III}(Hp_{-3H})(H_2O)_2]\cdot H_2O$ (where Hp = hematoporphyrin IX (7,12-bis(1-hydroxyethyl)-3,8,13,17-tetramethyl-21H-23H-porphyn-2,18-dipropionic acid)) and Hp-$_{3H}$ is the threefold deprotonated form of the Hp) have shown biological activity against a panel of leukemic cell lines (BV-173 and LAMA-84 cells [23]) and are as active as the leading Pt^{II} anticancer drug, cisplatin. Other reported uses of Pt^{III} complexes include applications as catalysts [24, 25] and organic light-emitting diodes (OLEDs).[26]

Stable Pt^{III} compounds are normally found as oligomers (Pt^{II}-Pt^{III})[27-29] or dimers containing a Pt-Pt bond, [24, 30] and/or bridging ligands.[17, 31, 32] However, stable Pt^{III} mononuclear species are known.[33-37] The first mononuclear Pt^{III} complex was reported in 1984 by Uson *et al.*[34], who synthesized $[(NBu_4)Pt^{III}(C_6Cl_5)_4]$ by oxidation of $[(NBu_4)_2Pt^{II}(C_6Cl_5)_4]$ with Cl_2 or Br_2 in CCl_4 solution. Later, an EPR study of $[(NBu_4)Pt^{III}(C_6Cl_5)_4]$ was reported where charge transfer from the ligand to Pt^{III} was proposed. As an alternative to oxidation of Pt^{II} complexes, the Pt^{III} state also is in principle accessible by reduction of Pt^{IV} complexes. The mode of action of cisplatin-based Pt^{IV} prodrugs requires reduction to their active Pt^{II} analogue via the loss of axial ligands.[38] Reduction of the Pt^{IV} prodrug $[Pt(NH_3)_2(CH_3COO)_2Cl_2]$ to a transient Pt^{III} intermediate has been examined theoretically using density functional theory (DFT).[39] Another computational study rationalized the redox instability of the Pt^{III} intermediate formed during the reduction of $Pt^{IV}(NH_3)_2Cl_2L_2$ to $Pt^{II}(NH_3)_2Cl_2$ (L = CH_3COO^-; $CHCl_2COO^-$; Cl^-). In particular, it was shown that electron transfer and the cleavage of the Pt−L bond occur in a stepwise fashion rather than being concerted and that the putative Pt^{III} species was easy to reduce to Pt^{II}. [40] The stability of the four coordinated Pt^{III} state can also be enhanced by shielding both axial positions to inhibit oxidative addition reactions. [41] Similarly, axial position protection achieved by agostic interactions contribute to the stability of ([Pt{(*p*-

$BrC_6F_4)NCH_2CH_2NEt_2\}Cl(py)]^+$ formed by electrochemical oxidation of ([Pt{(*p*-$BrC_6F_4)NCH_2CH_2NEt_2\}Cl(py)]$. [42, 43]

Anticancer agents containing Pt also have been reported to interact and disturb the oxidant-antioxidant homeostasis system strongly. [44, 45] Since anticancer Pt drugs can undergo redox processes in a cellular environment leading to alteration in their charge, geometry, and reactivity, [44, 46, 47] redox understanding of anticancer Pt drug behavior is critical.

The synthesis and characterization of *Class 2* Pt^{II} anticancer agents [Pt{(*p*-$YC_6F_4)N(R)CH_2CH_2NR'_2\}X(py)]$ (Y = H, F, Br; R = polyfluoroaryl; R' = Et, Me; and X= Cl, Br, I) has been reported in several studies from Monash University. [42, 48-51] The electrochemical oxidation of some of these materials has shed light upon conditions favoring the formation of formally monomeric Pt^{III} derivatives. [42, 43] Electrochemically reversible and close to chemically reversible one-electron oxidation processes have been reported for the anticancer compounds $[Pt^{II}\{(p\text{-}BrC_6F_4)NCH_2CH_2NEt_2\}Cl(py)]$, **1** [42] and $[Pt^{II}\{(p\text{-}HC_6F_4)NCH_2CH_2NEt_2\}Cl(py)]$, **2** [43] under short-timescale (fast scan-rate) cyclic voltammetric conditions at 23 °C in dichloromethane. However, instability of these formally Pt^{III} products is evident under both slow scan rate cyclic voltammetric and longer timescale bulk electrolysis conditions. Nevertheless, well defined frozen solution EPR spectra were obtained from the small residual concentrations of $[Pt\{(p\text{-}BrC_6F_4)NCH_2CH_2NEt_2\}Cl(py)]^+$, $\mathbf{1}^+$ and $[Pt\{(p\text{-}HC_6F_4)NCH_2CH_2NEt_2\}Cl(py)]^+$, $\mathbf{2}^+$ remaining after bulk oxidative electrolysis of $[Pt\{(p\text{-}BrC_6F_4)NCH_2CH_2NEt_2\}Cl(py)]$, **1** and $[Pt\{(p\text{-}HC_6F_4)NCH_2CH_2NEt_2\}Cl(py)]$, **2** in the non-coordinating CH_2Cl_2 (0.03 M $[Bu_4N][B(C_6F_5)_4]$) medium. Pt hyperfine interactions were obtained in the frozen solution EPR spectra of $\mathbf{2}^+$. The *g* values of $\mathbf{1}^+$ and $\mathbf{2}^+$ are consistent with the $5d^7$ ion Pt^{III} being in an elongated tetragonal environment with the unpaired electron in the $5d(z^2)$ orbital. Estimates of the $5d(z^2)$ character of around 32% and 37% in $\mathbf{1}^+$ and $\mathbf{2}^+$ respectively were obtained by crystal field calculations consistent with substantial delocalization of the unpaired electron onto the orbitals of the surrounding ligands. Thus $\mathbf{1}^+$ and $\mathbf{2}^+$ represent substantially delocalized systems implying that the choice of the ligand is probably vital in determining the extent of electron delocalization in this class of monomeric formally Pt^{III} species.

The present study reports the electrochemical oxidation of a Pt^{II} complex containing an unsaturated ligand [Pt{(*p*-BrC_6F_4)NCH=C(Cl)NEt_2}Cl(py)], **1Cl**. This complex was obtained as a major product from the chemical oxidation of anticancer agent **1** with hydrogen peroxide.[52] This outcome contrasts the formation of the Pt^{IV} complex [Pt{(*p*-HC_6F_4)NCH_2}$_2$(py)$_2$(OH)$_2$] on oxidation of [Pt{(*p*-HC_6F_4)NCH_2}$_2$(py)$_2$] with hydrogen peroxide.[53] The structures of crystallographically characterized **1** (trans-chlorido[N,N-diethyl-N′-(4-bromo-2,3,5,6-tetrafluorophenyl)ethane-1,2-diaminato(1-) pyridineplatinum(II),) and **1Cl** (trans-chlorido[N,N-diethyl-N′-(4-bromo-2,3,5,6-tetrafluorophenyl)-1-chloroethene-1,2-diaminato(1-) pyridineplatinum(II)) are given in **Scheme 1**.

Scheme 1. Platinum(II) complexes **1** and **1Cl**.

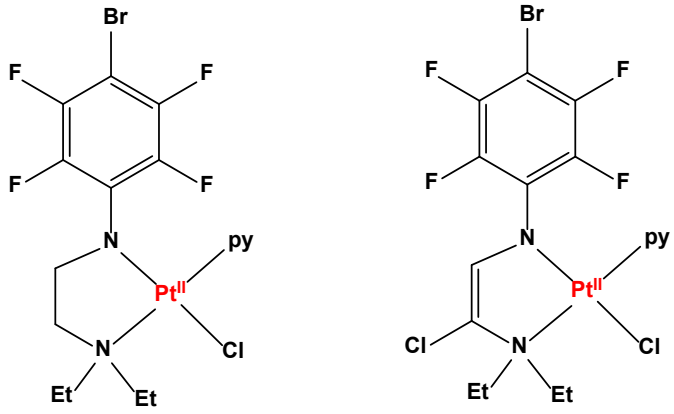

1 **1Cl**

Voltammetry, bulk electrolysis, *in situ* visible and IR spectroelectrochemical studies, and EPR studies on the one-electron oxidation of **1Cl** in dichloromethane (0.10 M [Bu_4N][PF_6]) reveal that the presence of an unsaturated ligand with a chloro substituent leads to a far more stable complex [Pt{(*p*-BrC_6F_4)NCH=C(Cl)NEt_2}Cl(py)]$^+$, $\mathbf{1Cl}^+$ relative to $\mathbf{1}^+$ and $\mathbf{2}^+$. EPR and XAFS studies as well as DFT calculations have been undertaken to assess the extent of electron delocalization in $\mathbf{1Cl}^+$. All data reveal that the extent of the delocalization of the unpaired electron onto the ligand is enhanced relative to that on $\mathbf{1}^+$ and $\mathbf{2}^+$, suggesting that this may be the reason for the enhanced stability of $\mathbf{1Cl}^+$.

Experimental

Synthesis

1Cl was synthesized as described in reference 52.

Electrochemistry

All voltammetric and bulk electrolysis experiments were undertaken in a glove box. Synthesis and purification of the $[Bu_4N][PF_6]$ supporting electrolyte, solvent purification, and electrodes and instrumentation for voltammetric and bulk electrolysis experiments are as reported in reference 43.

In an attempt to obtain crystals suitable for X-ray structural analysis, the purple-colored solution obtained after oxidative bulk electrolysis of **1Cl** in CH_2Cl_2 (0.10 M $[Bu_4N][PF_6]$) was kept under nitrogen at low temperature (−30 °C or −80 °C) following a small level of concentration by evaporation of the CH_2Cl_2 under vacuum. However, no crystals were obtained in any of these experiments and after 30 days, the color of the solution started to change from purple to orange. Crystallization was also attempted without initial evaporation and after substantial evaporation of the solvent, which enhanced the rate of color change to orange. In other unsuccessful attempts, n-hexane was added before attempting crystallization at lower temperatures. Complete evaporation of the solvent only gave crystalline electrolyte. Apparently, $\mathbf{1Cl}^+$ does not retain its high stability on the removal of the solvent.

DFT Calculations

Gaussian 16 [54] was used at the B3LYP [55-59] level of density functional theory (DFT) for geometry optimization. The Stuttgart Dresden (SDD) basis set and effective core potential were used for the platinum and chlorine atoms,[60] while the 6-31+G(d) all-electron basis set was used for other atoms. Spin densities were computed with NBO6.[61]

Visible and IR Spectroelectrochemistry

A PAR Model 362 scanning potentiostat supported by a PowerLab 4/20 interface and EChem software (version 1.5.2, AD Instruments) was used to control potentials during Visible and IR spectroelectrochemical (SEC) measurements. IR spectra were recorded using a BioRad FTS 175C FTIR spectrometer equipped with a Ge/KBr beam splitter and a high-sensitivity narrow-band MCT detector. The Visible spectra were collected using an Oriel Instaspec II linear diode

array (LDA) connected to an Oriel 127i 1/8 m spectrograph fitted with a 25 μm slit and a 300 line mm^{-1} grating with a 50 W, 12 V projector lamp as the light source. The optical arrangement gives a near-normal angle of incidence of the incident radiation to the planar working electrode (78°) for both IR and UV-Vis experiments. [62]

Spectroscopic measurements were obtained in the absorption/reflection mode, with the interrogating beam directed at near-normal incidence through the CaF_2 window and focused on the 3 mm diameter disk working electrode. A solution path length of 10-20 μm was sufficient to give a well-defined spectroscopic response while allowing rapid electrolysis in the thin film of solution in contact with the working electrode. The cell used for spectroelectrochemistry experiments has previously been described [62, 63]

The electrode assembly consisted of a 3 mm diameter Pt or glassy carbon (GC) disk working electrodes, an Ag wire quasi-reference electrode (QRE), and a Pt foil counter electrode. The reversible potential of the $Fc^{0/+}$ couple (Fc = ferrocene = $Fe(\eta^5\text{-}C_5H_5)_2$) is ca. 0.50 V vs. Ag QRE. The working electrodes were polished first on 9 mm, then 0.3 mm alumina-impregnated polishing film (Buehler), washed with distilled water, sonicated for 5 min, and dried thoroughly before use. After assembly, the SEC cell was placed in a dry box (under nitrogen and operated under elevated pressure, ca. 300 kPa), filled with 1.0 ml of a 5.0 mM **1Cl** solution in CH_2Cl_2 (0.10 mM $[Bu_4N][PF_6]$).

X-ray Absorption Spectroscopy (XAS)

A modified version of an X-ray absorption spectroscopy spectroelectrochemical (XAS-SEC) flow electrosynthesis cell developed for room temperature *in situ* XAS measurements [64] was used to prepare samples for low-temperature XAS and EPR measurements. Full operational details are provided in the Supporting Information.

EPR spectroscopy

EPR spectra were obtained at 298 K (solution phase) and at ca. 100 K (frozen solution) using a Bruker ER500 spectrometer. Simulations were undertaken with EASYSPIN[65] or Bruker SIMFONIA software. Generation of $\mathbf{1Cl}^+$ was undertaken by oxidation of **1Cl** (1.02 mM) in CH_2Cl_2 (0.30 mM $[Bu_4N][PF_6]$) in the flow electrosynthesis cell used for XAS measurements (*vide infra*). To undertake EPR experiments, the solution flow from the working electrode was

diverted to the EPR sample tube after exhaustive oxidation of **1Cl** which was marked by a change of solution color from pale yellow to blue/violet. Initially, the room-temperature solution-phase EPR spectra were recorded. Subsequently, the solution was frozen in liquid nitrogen and loaded into a Wilmad WG-850-B-Q nitrogen Dewar flask installed in the cavity of the EPR spectrometer.

Results and discussion

Electrochemical oxidation of 1Cl

Voltammetry of 1Cl in CH_2Cl_2 (0.10 M $[Bu_4N][PF_6]$)

Steady-state microelectrode voltammetry. In dichloromethane (0.10 M $[Bu_4N][PF_6]$), a very well-defined sigmoidal-shaped voltammogram is obtained at a Pt microelectrode (10 µm diameter), as shown in **Figure 1a**. Under these near steady-state conditions, the influence of iR_u drop (i = current, R_u = uncompensated resistance) is negligible, even in a high resistance solvent like CH_2Cl_2.

The number of electrons transferred per molecule in the oxidation process is confirmed to be one since a plot of E vs $\log_{10}(I_L\text{-}i/i)$ is linear with a slope ($2.303RT/nF$) equal to (57 ± 2) mV, where E = potential, I_L= limiting current and R, T, n and F have their usual meanings. The half-wave potential ($E_{1/2}$), calculated at $E = I_L/2$, is 355 ± 5 mV vs $Fc^{0/+}$. The use of the Saito equation that applies to the steady-state diffusion-controlled limiting current at a microelectrode [66] gives a diffusion coefficient (D) value of 8.2 x10^{-6} cm^2s^{-1}.

Transient cyclic voltammetry. Under transient cyclic voltammetric conditions at a macrodisk Pt electrode with a slow scan rate (20 mVs^{-1}), a reversible one-electron **1Cl/1Cl**$^+$ process also is obtained, as shown in **Figure 1b**. In cyclic voltammograms of **1** and **2** obtained at scan rates < 100 mVs^{-1}, a small oxidative shoulder with a reductive counterpart is evident after the initial one-electron oxidation process.[42, 43] In contrast, there is no follow-up chemical process evident after oxidation of **1Cl** even at a very slow scan rate, which implies that **1Cl**$^+$ is significantly more stable than **1**$^+$ or **2**$^+$.

Cyclic voltammetric data obtained as a function of scan rate are shown in **Figure 1c**, and data obtained from these experiments are summarised in **Table S1**. The magnitude of the i_p^{red}/i_p^{ox}

peak current ratio (i_p^{ox} = oxidation peak current, i_p^{red} = reduction peak current) is close to unity at all scan rates examined, confirming the chemical reversibility of the **1Cl/1Cl**$^+$ process. The midpoint potential E_m is 369 ± 5 mV vs. $Fc^{0/+}$, calculated from the average of the oxidation and reduction peak potentials $(E_p^{ox} + E_p^{red})/2$, which is similar to the $E_{1/2}$ value derived from steady-state voltammetry. The peak-to-peak separation ($\Delta E_p = E_p^{ox} - E_p^{red}$) obtained at low scan rates is close to the theoretically predicted value for a reversible process of 56 mV [66] at 23 °C. The increase in ΔE_p at higher scan rates is predominantly attributed to larger currents and hence enhanced *iRu* drop in the highly resistive CH_2Cl_2 medium. All data imply that a chemically and electrochemically reversible one-electron oxidation of **1Cl** to **1Cl**$^+$ occurs in CH_2Cl_2 (0.10 M $[Bu_4N][PF_6]$) under cyclic voltammetric conditions. Data obtained at a platinum macrodisk electrode were essentially the same as at a GC electrode.

Clearly, oxidation of **1Cl** to **1Cl**$^+$ is reversible under both steady-state microelectrode and transient macrodisk electrode conditions in CH_2Cl_2 (0.10 M $[Bu_4N][PF_6]$). Thus, the formally $Pt^{II/III}$ process can be described by the electrochemical (E) step (equation 1) with no evidence for a chemical (C) step (equation 2) following the electron transfer process as reported for related complexes. [42, 43, 67] The oxidation of **1Cl** exhibits the same ideal characteristics found for the known reversible one-electron oxidation of Fc to Fc^+ under both steady-state and transient voltammetric conditions.

E $Pt^{II} \rightleftharpoons Pt^{III} + e^-$ **(1)**

C $Pt^{III} \xrightarrow{\text{slow}} \text{Product(s)}$ **(2)**

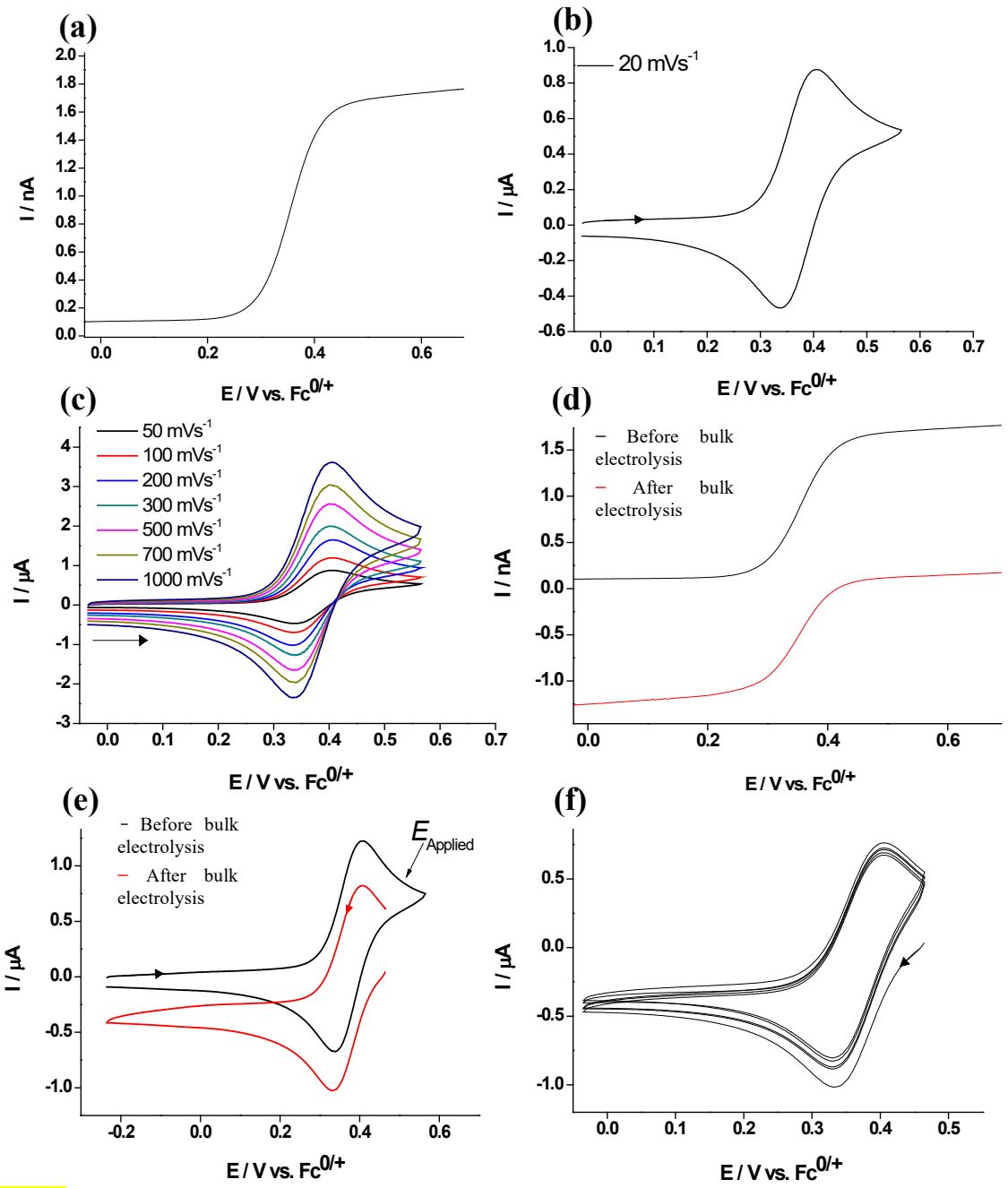

Figure 1. (a) Near steady-state voltammogram obtained at a 10 µm diameter Pt microdisc electrode at a scan rate of 10 mVs^{-1} for oxidation of **1Cl** (1.02 mM) in CH_2Cl_2 (0.10 M $[Bu_4N][PF_6]$) **(b)** Transient cyclic voltammogram for oxidation of **1Cl** (0.90 mM) obtained at Pt macrodisc electrode (A = 0.0093 cm^2) in CH_2Cl_2 (0.10 M $[Bu_4N][PF_6]$)]) at a scan rate of 20 mVs^{-1} **(c)** Transient cyclic voltammograms for oxidation of **1Cl** (0.90 mM) obtained at a Pt macrodisc electrode (A = 0.0093 cm^2) in CH_2Cl_2 (0.10 M $[Bu_4N][PF_6]$) at designated scan rates. **(d)** Steady-state voltammograms obtained at a 10 µm diameter Pt microelectrode before (−) and after (−) bulk electrolysis of **1Cl** (1.02 mM) at a Pt mesh electrode in CH_2Cl_2 (0.10 M $[Bu_4N][PF_6]$) **(e)** cyclic voltammograms obtained at Pt macrodisk electrode (A = 0.0093 cm^2) with a scan rate of 100 mVs^{-1} before (−) and after (−) the bulk electrolysis of **1Cl** (1.02 mM) in CH_2Cl_2 (0.10 M $[Bu_4N][PF_6]$) **(f)** Cyclic voltammograms obtained at a Pt macrodisk electrode (A = 0.0093 cm^2) with multiple cycling of the potential at the scan rate of 100 mVs^{-1} after bulk electrolysis of **1Cl** (1.02 mM) in CH_2Cl_2 (0.10 M $[Bu_4N][PF_6]$).

Bulk oxidative electrolysis of 1Cl

An exhaustive bulk oxidative electrolysis experiment was undertaken with 8 ml of 1.02 mM **1Cl** in CH_2Cl_2 (0.10 M $[Bu_4N][PF_6]$) using a platinum mesh electrode held at a potential of 0.57 V vs $Fc^{0/+}$. During electrolysis, the solution color changed from yellow to deep violet – purple. The number of electrons transferred (n-value) for the oxidation process was determined to be 0.95± 0.03 based on coulometric analysis of the current-time data.

The near steady-state voltammogram obtained at the 10 µm diameter Pt microelectrode for oxidation of **1Cl** (1.02 mM) before bulk electrolysis contains only positive Faradaic current (**Figure 1d**). After oxidative bulk electrolysis, the $\mathbf{1Cl}^{0/+}$ oxidation process is replaced by a $\mathbf{1Cl}^{+/0}$ reduction process (**Figure 1e**), having only negative current but with the same $E_{1/2}$ value as for reduction of **1Cl**. The similar magnitudes of the limiting currents before and after bulk electrolysis are as expected for a high yield of stable $\mathbf{1Cl}^{+}$. Cyclic voltammograms obtained before and after bulk electrolysis of **1Cl** are presented in **Figure 1e** and again reveal the transition from reversible oxidation to a reversible reduction process. Cyclic voltammograms obtained after the bulk electrolysis using multiple cycling of the potential (**Figure 1f**) display the theoretically expected small decrease in the magnitude of the current with each cycle, but no new processes emerge. All these data confirm that $\mathbf{1Cl}^{+}$ remains fully stable even under long-timescale bulk electrolysis conditions, unlike $\mathbf{1}^{+}$ and $\mathbf{2}^{+}$ generated via bulk electrolysis of **1** and **2**. [42, 43] After many attempts, single crystals of $\mathbf{1Cl}^{+}$ could not be obtained from the oxidized solution obtained after the bulk electrolysis, even at low temperatures (see experimental)

Density functional theory (DFT) study on the $\mathbf{1Cl}^{0/+}$ and $\mathbf{1}^{0/+}$ processes

DFT calculations relevant to the $\mathbf{1Cl}^{0/+}$ process proceeded by geometry optimization of **1Cl** using the X-ray derived coordinates of the solid as a starting geometry, followed by re-optimization of the geometry of the $\mathbf{1Cl}^{+}$ cation as a spin doublet. The optimized geometries and natural spin densities of the singly occupied molecular orbital (SOMO) for $\mathbf{1Cl}^{+}$ are summarised in **Figure 2**. The predicted bond lengths and bond angles of the theoretical models of **1Cl** and $\mathbf{1Cl}^{+}$ and those obtained from the X-ray crystal structure of **1Cl** are provided in **Tables S2** and **S3**. Analogous results for the $\mathbf{1}^{0}$ and $\mathbf{1}^{+}$ pair are provided in **Figure S1** and **Tables S2** and **S3**.

The highest occupied molecular orbitals (HOMO) for each neutral and SOMO for the oxidized forms in **1** and $\mathbf{1}^+$, and **1Cl** and $\mathbf{1Cl}^+$ pairs are similar. Both $\mathbf{1}^+$ and $\mathbf{1Cl}^+$ have an unpaired electron which can be distributed in terms of charge densities over the metal and ligand framework. Thus, $\mathbf{1}^+$ has spin densities 0.55 and 0.28 e/Å^3 at the amide nitrogen and platinum (**Figure S1**). However, for $\mathbf{1Cl}^+$, containing the unsaturated skeleton, the electron density for the SOMO is primarily at the amide nitrogen, C7 and C8 with spin densities 0.39, −0.12, and 0.40 e/Å^3, respectively, and only 0.13 e/Å^3 on platinum (**Figure 2**). Clearly, the electron density lies predominantly on the ligand framework for $\mathbf{1Cl}^+$ and this is suggested to be a major reason for its enhanced stability relative to $\mathbf{1}^+$.

The geometry around the Pt center is planar, with the sum of the four X-Pt-X angles being 360° for **1**, $\mathbf{1}^+$, **1Cl,** and $\mathbf{1Cl}^+$. In the case of the **1Cl** and $\mathbf{1Cl}^+$ couple, small changes in the coordination geometry of the metal are predicted following oxidation, such as a shortening of the Pt-N1 and Pt-Cl bonds and a lengthening of the Pt-N2 and the C=C bond of the chelating ligand. Clearly, the impact of oxidation significantly impacts the unsaturated ligand framework.

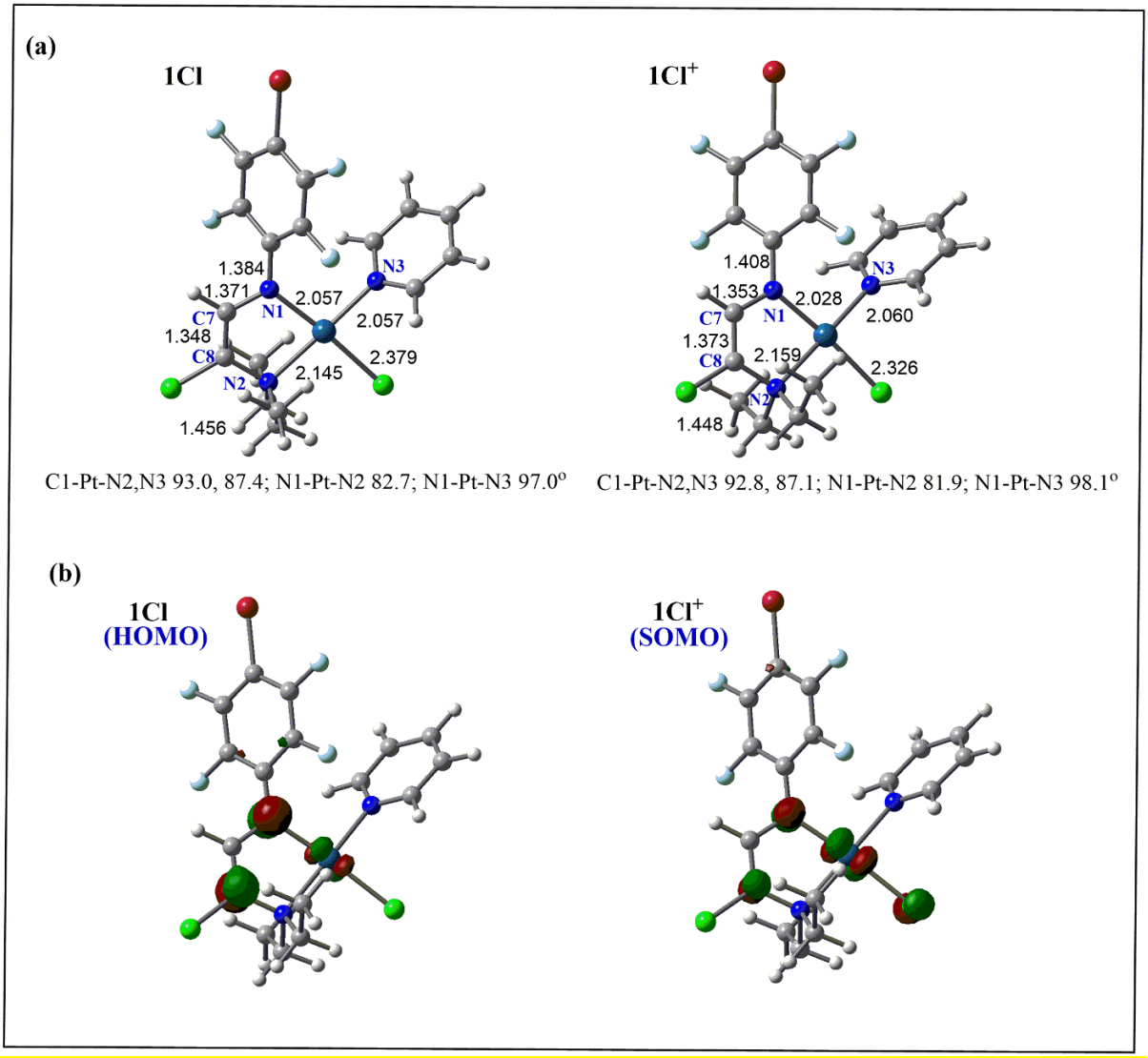

Figure 2. (a) Gaussview diagram for **1Cl** and **1Cl**$^+$ **(b)** HOMO of **1Cl** and SOMO of **1Cl**$^+$ illustrating the impact of the delocalization of the unpaired electron on the unsaturated ligand skeleton. Atom color code: Red (Br), light blue (F), blue (N) and cyan (Pt).

Spectroelectrochemical (SEC) studies on 1Cl

In situ visible spectroscopy

Spectroelectrochemical experiments at visible wavelengths were undertaken using the thin layer reflection-absorption cell, which maintained the sample in an anaerobic (dinitrogen) environment. The reversible spectral changes in the visible region resulting from oxidation of **1Cl** to **1Cl**$^+$ followed by reduction of electrogenerated **1Cl**$^+$ back to **1Cl** are shown in **Figure 3**. The spectra are displayed in the differential absorbance format where the initial spectrum, measured at the resting potential of the system, is used as the reference. Application of a potential of 1.0 V vs. the Ag QRE for 16 s resulted in quantitative oxidation of **1Cl** to **1Cl**$^+$

(**Figure 3 top**). The chemical reversibility of the oxidation process was established by recovery of the initial spectrum following the return of the initial potential to 0.0 V vs Ag QRE for 40 s, which achieved a complete reduction of electrochemically generated **1Cl**$^{+}$ back to **1Cl** (**Figure 3 bottom**). The presence of a well-defined isosbestic point at 467 nm for both the oxidation and reduction steps is consistent with the direct interconversion of the redox partners. The crossover region in absorbance in the 381 nm region is slightly less well defined, most likely due to the poorer photometric accuracy of the system at shorter wavelengths and the higher absorbance of the sample. The robust character of the system to redox cycling was demonstrated by the application of ten oxidation/reduction cycles, where each cycle was marked by a very high level of reversibility. In summary, the **1Cl/1Cl**$^{+}$ system is chemically reversible on the timescale of the thin layer Visible SEC experiment.

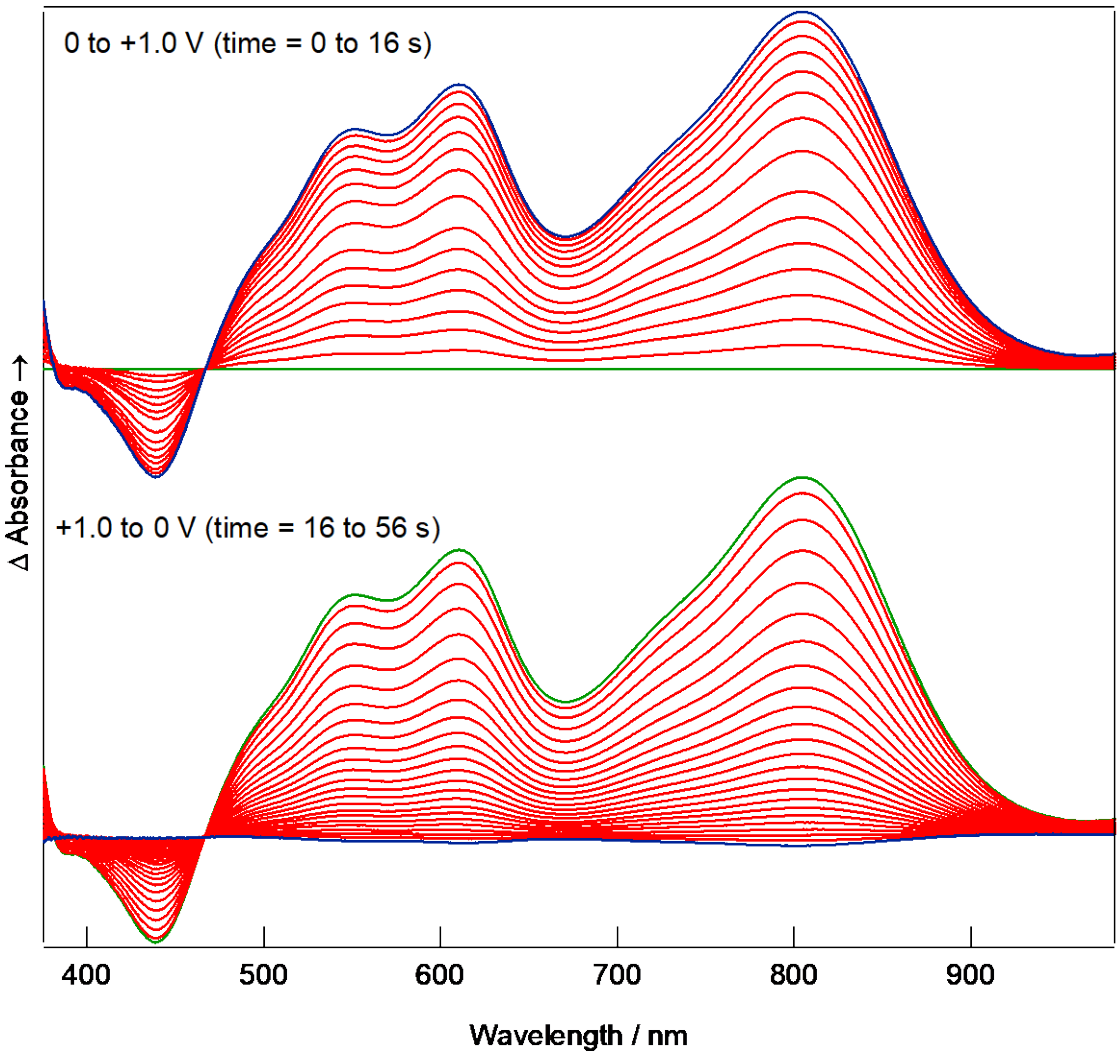

Figure 3. Differential absorbance spectra in the visible region obtained during the course of oxidation of 5.0 mM **1Cl** in CH_2Cl_2 (0.1 M $[Bu_4N][PF_6]$) (top) to $\mathbf{1Cl}^+$ and reduction of electrochemically generated $\mathbf{1Cl}^+$ back to **1Cl** (bottom). The first recorded spectrum was used as the background for subsequent spectra. The film thickness was approximately 10 µm and the reference corresponds to the spectrum recorded immediately prior to application of the oxidizing potential. Spectra were collected at intervals of 1.1 s. The initial and final spectra of each set are plotted in green and blue, respectively.

In situ IR spectroelectrochemistry

Complete reversal of the intensity in IR SEC spectra recorded during oxidation of **1Cl** to $\mathbf{1Cl}^+$ and reduction of electrochemically generated $\mathbf{1Cl}^+$ back to **1Cl** is displayed in **Figure 4**. The presence of multiple isosbestic points is evident. Low transmittance of the single beam spectra, associated with strong absorption by the solvent and supporting electrolyte, limits the reliability of interpretation of the IR spectra in the regions of 1473-1420 cm^{-1} and 1290-1235 cm^{-1}.

Accordingly, these regions are blocked out in **Figure 4**. **Figure S2** provides the time evolution of the product concentrations during oxidation of **1Cl** to $\mathbf{1Cl}^+$ and then reduction of $\mathbf{1Cl}^+$ back to **1Cl** for two IR bands. The band at 1501 cm^{-1} increases with time as $\mathbf{1Cl}^+$ is generated in the course of oxidation of **1Cl**. An exactly equivalent decrease with time occurs on the reduction of $\mathbf{1Cl}^+$ back to **1Cl**. Conversely, the band at 1620 cm^{-1} shows a decrease with time and reflects the consumption of **1Cl** during the oxidation and its recovery on reduction. This SEC behavior again confirms that the electrochemical oxidation of $\mathbf{1Cl}^+$ to **1Cl** is a chemically reversible process. The fact that changes in frequency during oxidation are only small also implies that $\mathbf{1Cl}^+$ is structurally similar to its Pt^{II} precursor **1Cl**.

DFT calculations provide a basis for the interpretation of the IR spectra. The bands of **1Cl** in the 1100 to 1800 cm^{-1} region are dominated by skeletal modes of the ligands and, while subject to basis set-dependent scaling errors, give a satisfactory representation of the observed spectrum. Experimentally, the IR difference spectrum (**1Cl** - $\mathbf{1Cl}^+$) is well defined and provides a sensitive test of the calculated differences in structural parameters and force constants associated with the one-electron oxidation process. While the calculated normal modes have displacement coordinates involving many atoms, particular atom displacements dominate the character of the modes. Several key modes are illustrated in **Figure 4c** and involve the translation of the enamide N atom about the three bonds to this atom, a breathing mode of the perfluoro ring, and a C=C stretch of the enamide. The differing sensitivity of these modes to oxidation will be related to the enamide domination of the SOMO (Figure 4). Based on their relative intensities and wavenumbers, bands associated with the translation of the enamide N atom along the three bond directions may be identified at 1142, 1223, and 1316 cm^{-1} for **1Cl** (**Figure 4**). The shift in wavenumber and intensity of the corresponding bands following oxidation give distinctive signatures in the calculated differential absorption spectra and these predictions match closely with the observed spectra. The expected lengthening of the C=C bond of the enamide on oxidation of **1Cl** to $\mathbf{1Cl}^+$ (**Figure 4**) is predicted to lead to a significant change in the modes. Stretching of this bond is assigned to the band at 1644 cm^{-1}. The 1798 cm^{-1} mode of **1Cl** is calculated to shift to 1480 cm^{-1} for $\mathbf{1Cl}^+$, although the form of the normal mode is more mixed for the cation. The band at 1405 cm^{-1} has an intensity and half-width consistent with its assignment to this mode and the relative wavenumbers of the bands for the

neutral and cationic species also support the assignment. The ring breathing modes of the perfluorophenyl substituent occur near 1620 cm^{-1} and the calculations suggest smaller changes in wavenumber and relative intensity for these modes. The most intense bands in the spectral region under consideration, between 1473 and 1520 cm^{-1}, are due primarily to the C-C-H bending vibrations of the ethyl groups. The calculated spectra predict small shifts in wavenumber and relative intensity and give rise to the largest changes in the differential absorption spectra. In summary, the differential absorption IR spectra recorded during oxidation of **1Cl** to **1Cl**$^+$ and subsequent reduction of **1Cl**$^+$ **back to 1Cl** confirm that the process is chemically reversible and that the spectral changes can be closely matched to those calculated for the interconversion of **1Cl** and **1Cl**$^+$.

Specific assignments of the IR bands have been discussed for the polyfluoroaryl and pyridine rings of the *Class 1* compound, [Pt{((p-HC_6F_4)NCH_2)$_2$}(py)$_2$], [68] and show that the normal modes are highly mixed and provide a fingerprint for these types of compounds. The use of differential absorption IR-SEC measurements has been used with ν(CO) modes to confirm the validity of calculated structures based [69] [70] This study provides a clear example based on the use of the more complicated spectral profile characteristic of the "fingerprint" region of the IR spectrum.

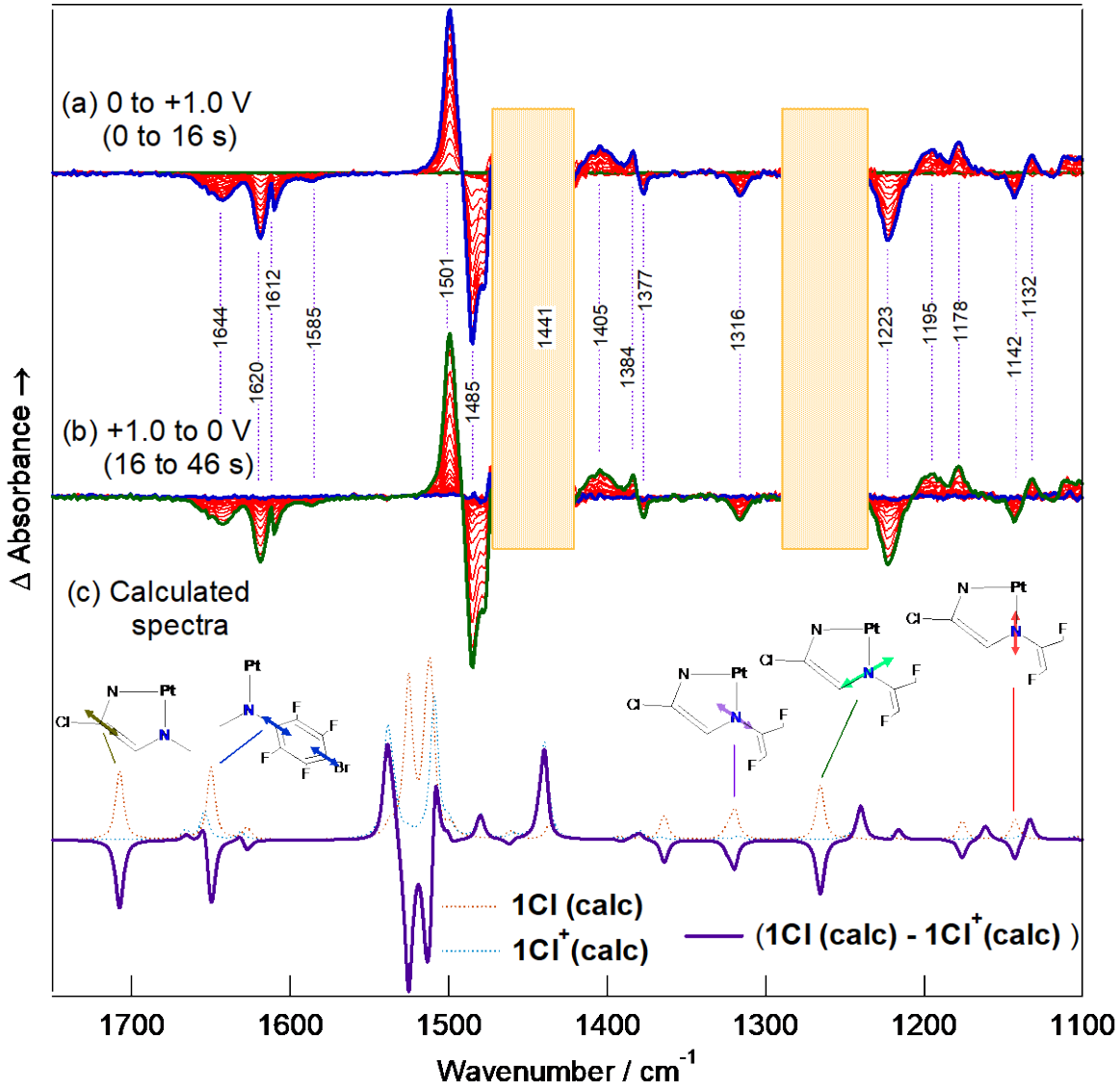

Figure 4. **(a)** IR SEC data for the oxidation of **1Cl** to **1Cl**$^{+}$ and **(b)** reduction of **1Cl**$^{+}$ back to **1Cl** using a thin layer containing 5.0 mM **1Cl** in CH_2Cl_2 (0.1 M $[NBu_4][PF_6]$). Initial and final spectra of each series are plotted in green and blue, respectively. Strong absorption by the solvent and supporting electrolyte prevent the collection of reliable data in the regions near 1450 and 1275 cm^{-1}. **(c)** The calculated spectra for **1Cl** and **1Cl**$^{+}$ and the calculated differential absorption spectra. All bands were calculated as Lorentzian (80%)/Gaussian (20%) profiles with a full width at half maximum value of 8 cm^{-1}.

EPR Spectroscopy of 1Cl^{+}

The high stability of **1Cl**$^{+}$ allows flow-based electrosynthesis to generate samples suitable for EPR measurements in the liquid phase at room temperature and frozen solutions at ca. 100 K.

Visual monitoring of the intensity of the blue color of the oxidized compound in the EPR tube, together with the current-time response, provided feedback on the progress of the electrochemical oxidation. The liquid phase (298 K) EPR spectrum of **1Cl**$^{+}$ derived from the oxidation of 1.02 mM **1Cl** in CH_2Cl_2 (0.10 M $Bu_4N[PF_6]$) is shown in **Figure 5**. The strongest feature of the spectrum, at ca. 338 mT, is attributed to an unpaired electron interacting with a nucleus of one of the three isotopes of Pt with the nuclear spin $I = 0$ (^{194}Pt 32.8%; ^{196}Pt 25.4%; ^{198}Pt 7.23%). The resonances at ~ 335 and ~ 343 mT result from the interaction of the unpaired electron with the nucleus of 33.7% abundant ^{195}Pt isotope with $I = ½$. The presence of the shoulder at g ~ 2.1 (ca. 332 mT) is indicative of the presence of a second species whose features may be discerned by subtraction of the simulated spectrum of the major species from the experimental spectrum. The spectrum of this second (minor) species is also included in **Figure 5**. We estimate that the major species contributes approximately 88 % and the minor species 12 % to the total spectral intensity. The main features of the spectrum of the major species were best fitted with isotropic g and hyperfine values of $g_0 = 2.0567$ and A_0 (^{195}Pt) 55.57 x 10^{-4} cm^{-1}. Small further improvements to the fit were obtained by the inclusion of hyperfine coupling to N and Cl nuclei as provided in **Table 1 and Figure S3** and discussed in the SI. A similar analysis was performed for the minor species. Although g_0 and ^{195}Pt A_0 for the major species can be regarded as well-established, the parameters for the small couplings to N and Cl nuclei and all parameters of the minor species must be interpreted with caution. In particular, the values of the small couplings to N and Cl nuclei are not well established, although the ORCA-based calculations suggest an ordering of the hyperfine constants of Pt >> N > Cl, as indeed estimated through simulations.

The EPR spectrum is consistent with the formation of a mixture of two structurally similar forms of **1Cl**$^{+}$**,** as also observed for **1Cl** in acetone by ^{195}Pt and ^{1}H NMR[43]. The identity of these two forms has not been firmly established for **1Cl**. In the case of **1Cl**$^{+}$, the differences in EPR, g, and A_{Pt} values could arise from differences in the interaction between the Pt and enamide ligands due to rotation of the plane of the perfluorophenyl substituent or from different interactions with the dichloromethane solvent. NMR and EPR spectra provide evidence for the presence of two closely related structural forms in both the reduced and oxidized forms of the platinum complex. In contrast, transient and steady-state voltammetric as well as visible and IR spectroelectrochemical data derived from electrolysis are fully consistent with a

straightforward fully reversible **1Cl**$^{0/+}$ process. This is expected if structurally similar species resolved on the very short timescale NMR and EPR measurements are in rapid equilibrium on the much longer electrochemical timescale. Furthermore, it is likely that the reversible potentials for all species are very similar, making their electrochemical resolution problematic.

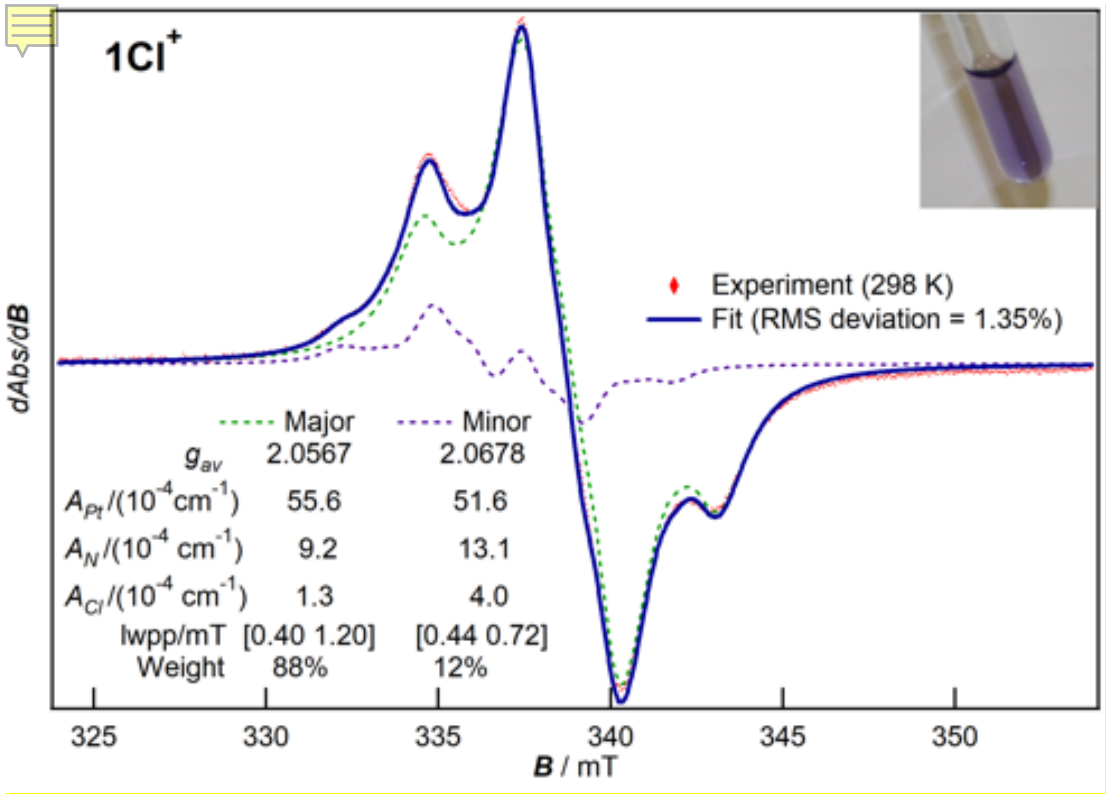

Figure 5. Solution phase X-band EPR spectrum of **1Cl**$^{+}$ obtained by bulk oxidative electrolysis of 1.02 mM **1Cl** in CH_2Cl_2 (0.10 M $[Bu_4N][PF_6]$ at 298 K and the simulated spectrum based on a two-species model with coupling to ^{195}Pt, N, and Cl nuclei as described in the text and using g and hyperfine interaction parameters as listed in Table 1. The inset picture is of the electrochemically oxidized **1Cl**$^{+}$ purple-colored sample. The **1Cl** solution prior to oxidation is pale yellow. The major species accounts for 88 % of the signal intensity and has linewidth parameters Iwpp/mT [0.42, 1.19] while the minor species accounts for 12 % and has linewidth parameters Iwpp [0.71, 1.18]. A comparison of fits of the experimental spectra to models, which include hyperfine coupling to Pt only and to Pt and N nuclei is given in the SI.

The interpretation of the spectrum of the frozen solution of **1Cl**$^{+}$ at 100 K also is complicated by resonances due to the minor species noted above in solution phase EPR spectra and possibly by other minor species in the field range 330 to 345 mT. The two highest g-values, associated with the lowest field resonances in the range 320 to 330 mT, were readily established by

simulation and the associated hyperfine interactions by constraining these to fit within the envelope of the experimental spectrum. The third g-value and its corresponding Pt hyperfine interaction could be most reliably established by making use of the isotropic g and A (g_0 and A_0 respectively) values obtained from the tumble averaged liquid phase spectrum. Thus we obtain the relevant g and A using $g_0 = (g_1+g_2+g_3)/3$ and similarly $A_0 = (A_1 + A_2 + A_3)/3$, where g_0 and A_0 are the isotropic g and hyperfine interactions obtained from the liquid phase spectrum. A simulation of the frozen solution spectrum, shown in **Figure 6**, required the inclusion of a contribution of about 12 % from the minor species. The $\langle g \rangle$, $\langle A_{Pt} \rangle$, $\langle A_N \rangle$ and $\langle A_{Cl} \rangle$ values are constrained to the values obtained for the major species (**Figure 5**). The labeling of the axes as 1, 2 or 3 is dependent on the character of the metal-based SOMO as discussed below. The difference in broadening of the g components is most simply modeled using strain broadening. However, it is noted that this approach is not unique, and highly anisotropic N and Cl hyperfine coupling can give similarly satisfactory simulations. In the absence of ENDOR measurements to support the magnitudes and anisotropy of the hyperfine coupling, the strain-broadening approach was used here. As can be seen from **Table 1**, the averages of the algebraic sums of the g_i and A_i obtained for the frozen solution spectrum are constrained to be within the experimental uncertainties of the values of g_0 and A_0 obtained from the liquid phase spectrum. This analysis indicates that all the components of A have the same sign. Use of the solution phase spectrum in this way leads to values of $g_3 = 1.999$ and $A_3 = 60.0 \times 10^{-4}$ cm^{-1}. Ref [71]

Spin density in the 5d(z^2) orbital. Spin density in the 5d orbital. The values of the components of g and A for the major species may be used to predict α^2, the contribution of the relevant *5d* orbital to the SOMO in **1Cl**$^+$ using theory and assumptions similar to those employed[39] with **1**$^+$. Details of the calculations are provided in the Supporting Information. Although we initially calculated α^2 on the basis of the SOMO being ***5d(z^2)***, obtaining $\alpha^2 = 0.10$, the DFT calculations lead to a SOMO of ***5d(xz)***. This leads to an ordering of the g-values of $g_1 < g_2 < g_3$ and thence to $\alpha^2 = 0.06$ (i.e. 6%). This range of value of 0.06 to 0.10 compares satisfactorily with the DFT estimate of 0.13 given that the EPR calculation is based on some significant assumptions and contains within it an estimated uncertainty of around 30%. This value of the spin density in the ***5d(z^2)*** orbital is smaller than that estimated for **1**$^+$ (32 % [42]) and **2**$^+$ (37 % [43]) but is similar to that (15% [72]) calculated from the EPR spectrum obtained by partial electrochemical oxidation of [Pt{((*p*-HC_6F_4)NCH_2)$_2$}(py)$_2$] in the study by Mason et al.[72] This, together with the smaller

g-anisotropy found with $\mathbf{1}^+$ and $\mathbf{2}^+$, suggests that the unpaired electron in $\mathbf{1Cl}^+$ is more delocalized onto the orbitals of the surrounding ligands and the system may better be regarded as a Pt(II) metalloradical. The more extreme delocalization may explain the higher stability of $\mathbf{1Cl}^+$ relative to that of $\mathbf{1}^+$ and $\mathbf{2}^+$.

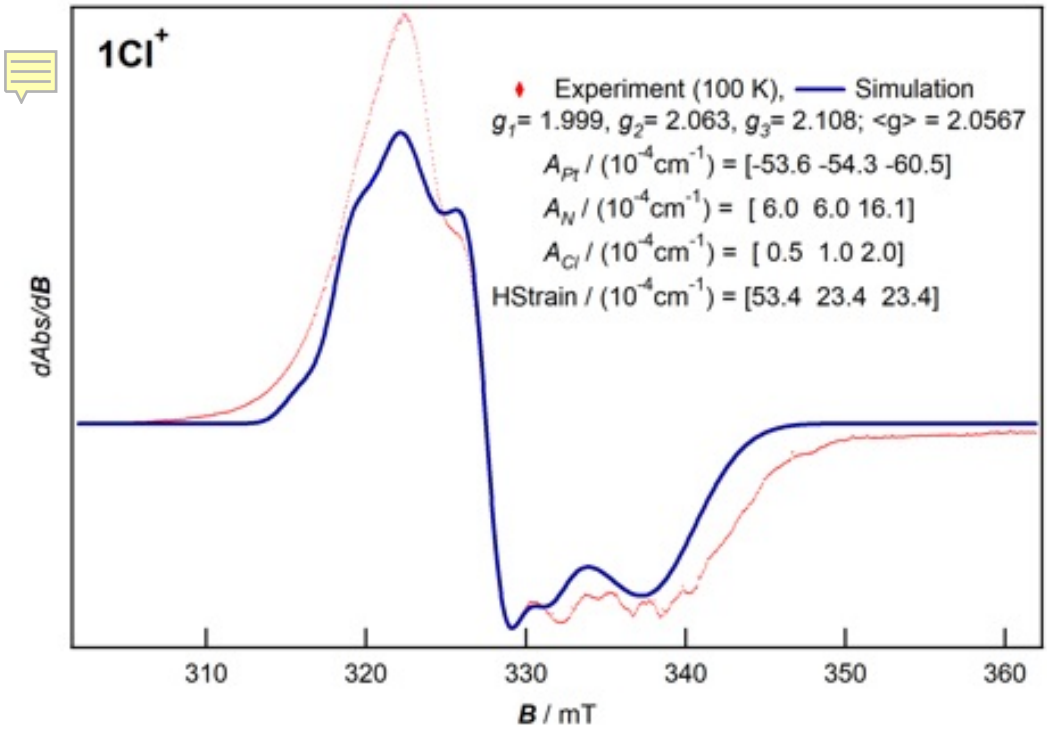

Figure 6. Frozen solution-phase X-band (9.494 GHz) EPR spectrum of $\mathbf{1Cl}^+$ at 100 K obtained by bulk oxidative electrolysis of 1.02 mM (**1Cl**) in CH_2Cl_2 (0.10 M $[Bu_4N][PF_6]$ and the simulated spectrum based on the major species as identified at 298 K with coupling to ^{195}Pt, N, and Cl nuclei as described in the text and using g, hyperfine interaction and linewidth parameters as listed in **Table 1**.

Table 1. Summary of the g and A (hyperfine) parameters used to simulate the liquid and frozen solution phases of the EPR spectra of $\mathbf{1Cl}^+$ as shown in **Figures 5** and **6** as described in the text. All hyperfine interaction and linewidth parameters are given in units of $\times 10^{-4}$ cm^{-1}.

	Solution phase major species	Solution phase minor species	Frozen solution 1	Frozen solution 2	Frozen solution 3
g	2.0567	2.0678	1.999	2.063	2.108
A(Pt)	55.6	51.6	−53.6	−54.3	−60.5
A(N)	9.2	13.1	6.0	6.0	16.1
A(Cl)	1.3	4.0	0.5	1.0	2.0
Frozen solution H Strain linewidths (see text)			53.4	23.4	23.4

X-ray Absorption Spectroscopy (XAS)

The DFT calculations suggest a small Pt-based contribution to the SOMO (ca. 13%). The EPR data suggest a metal contribution of around 6-10%. XAS measurements at the Pt-L_3 edge have been shown to be sensitive to the Pt oxidation state. This is manifested most clearly by the relative intensity of the Whiteline ($2p_{3/2} \rightarrow 5d$ transitions) where the intensity increases with the presence of more vacancies in the Pt d orbitals. [73] In particular, the normalized intensity of the Whiteline increases from 1.30 to 1.94 on going from Pt^0 (foil) to Pt^{IV} (H_2PtCl_6).

The normalized X-ray absorption near-edge spectra (XANES) of frozen solutions of **1Cl** and electrogenerated **1Cl**$^+$ are presented in **Figure 7**. The spectra are virtually identical apart from the relative intensity of the Whiteline, which increases from 1.60 to 1.65. This increase in normalized intensity is fully reproduced in three independently prepared samples. Despite the simplicity of the analysis, there is a good linear correlation between the normalized intensity of the Whiteline and the formal Pt oxidation state for Pt metal, **1Cl,** and H_2PtCl_6. The increased normalized intensity of the Whiteline of **1Cl**$^+$ corresponds to a small formal increase in oxidation state by 0.17. This result, along with high similarity in the shape profile in the XANES spectra, again suggests that predominantly ligand-based oxidation of **1Cl** has occurred

when forming **1Cl**$^+$, as also deduced from the EPR analysis of **1Cl**$^+$ and examination of the SOMO composition of **1Cl**$^+$ derived from DFT theory. As with voltammetric and Visible and IR spectroelectrochemical studies, no evidence of structurally similar forms of **1Cl** and **1Cl**$^+$ detected by NMR and EPR, respectively, is evident in the XANES data.

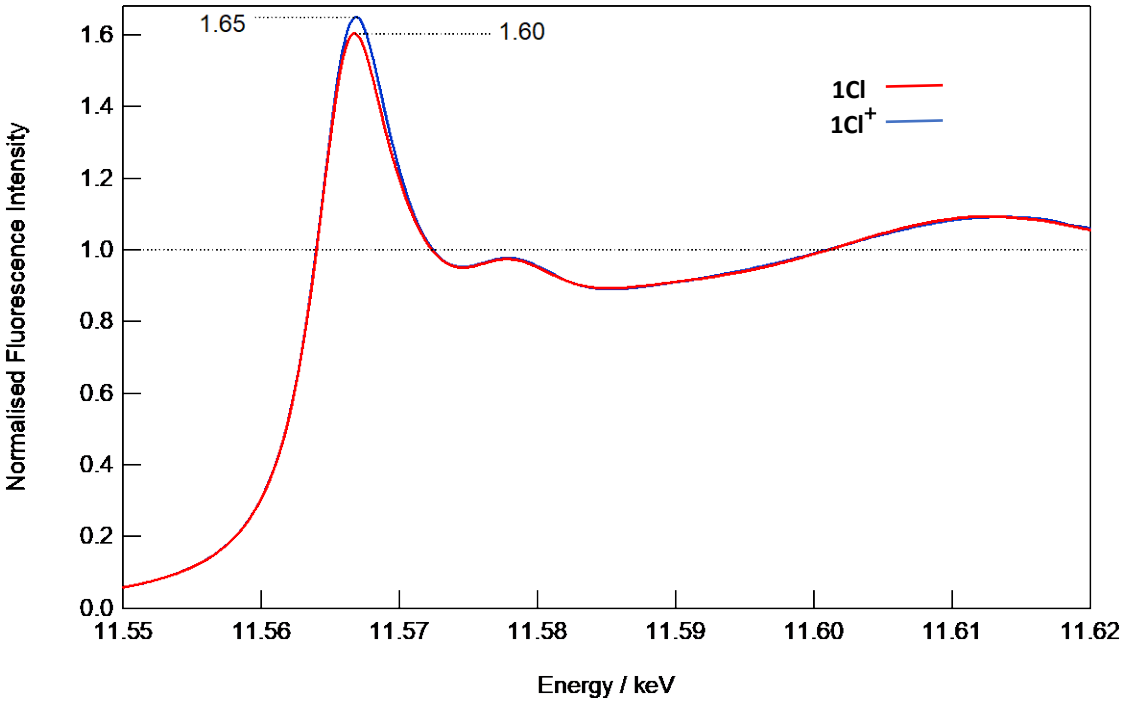

Figure 7 Pt L_3-edge frozen solution spectra obtained from **1Cl** (red) and **1Cl**$^+$ (blue).

Conclusion

The presence of the pre-oxidized ligand with a chloro substituent greatly increases the stability of the product formed by a one-electron electrochemical oxidation of **1Cl** [Pt^{II}{(*p*-BrC_6F_4)NCH=C(Cl)NEt_2}Cl(py)]) to **1Cl**$^+$ in CH_2Cl_2(0.10 M [$Bu_4N[PF_6]$]). The **1Cl/1Cl**$^+$ process displays electrochemical and chemical reversibility on the short timescale of cyclic voltammetry at GC and Pt electrodes. Stability is also maintained on the synthetically relevant and much longer timescale of bulk electrolysis which allows a high yield of stable **1Cl**$^+$ to be obtained in CH_2Cl_2 solution. Full chemical reversibility also is observed in IR and Visible spectroelectrochemical studies for the oxidation of **1Cl** to **1Cl**$^+$ and reduction of

electrochemically generated **1Cl**$^+$ back to **1Cl**. Since **1Cl**$^+$ could not be isolated as a solid and hence no X-ray crystal structure of **1Cl**$^+$ is available, DFT was used to probe the extent of electron delocalization on **1Cl**$^+$, indicating only a minor fraction of the electron density resides on the Pt metal center, implying that the **1Cl/1Cl**$^+$ process is extensively ligand-based. The high stability of **1Cl**$^+$ in CH_2Cl_2 enabled the solution phase as well as frozen solution EPR spectra to be recorded. The average g value for the frozen solution spectra 2.056 is significantly greater than that of 2.0023 expected for a free radical. Approximate analysis of the EPR spectra of **1Cl**$^+$ based on crystal field theory leads to an estimate of the $5d(z^2)$ character of around 6% to 10%. Analysis of X-ray absorption fine structure (XAFS) data obtained with frozen CH_2Cl_2 samples also supports the presence of delocalized singly occupied metal molecular orbital with a spin density on Pt, similar to that derived from EPR data.

This study leads to the conclusion that the stability of the formally Pt^{III} **1Cl**$^+$ complex containing a pre-oxidized ligand is enhanced by significantly greater delocalization of the unpaired electron onto the coordinated organoamide ligand relative to **1**$^+$ formed by oxidation of **1**([Pt^{II}{(*p*-BrC_6F_4)$NCH_2CH_2NEt_2$}Cl(py)]), in which the ligand is saturated.

Associated Content

Supporting Information

The Supporting Information is available free of charge at

https://pubs.acs.org/doi/10.1021/acs.inorgcem.--

XAS experimental details, a summary of cyclic voltammetric d data for **1Cl**, DFT calculations for **1** and **1**$^+$, bond lengths and bond angles obtained from the crystal structures (**1**, **1Cl**) and theoretical calculations (**1**, **1**$^+$, **1Cl**, **1Cl**$^+$), IR-SEC spectra for oxidation of **1Cl** to **1Cl**$^+$ and reduction of electrosynthesised **1Cl**$^+$ back to **1Cl** along with the time evolution of two ring stretch modes, crystal field analysis and fitting of EPR spectra of **1Cl**$^+$, and Cartesian coordinates derived from DFT optimizations have been provided.

Acknowledgments

AMB gratefully acknowledges financial support from the Australian Research Council. RO thanks the Australian Government for the provision of an Australian Postgraduate Award. The

ARC is thanked for funding the purchase of the EPR instrument (LE0775660). X-ray spectroscopy was performed using the XAS beamline at the Australian Synchrotron, Victoria, Australia, part of ANSTO, and DFT computation was enabled by access to the National Computing Infrastructure. We thank the beamline team and in particular, Dr. B. Johannessen, for assistance during those experiments. We gratefully acknowledge Dr. Shashank Vittal Rao and Assoc. Prof. Alessandro Soncini (University of Melbourne) for helpful discussions and for investigating ab initio calculations of the EPR spectra.

Conflict of interest

The authors declare no conflict of interest.

References

1. Bruijnincx, P. C.; Sadler, P. J., New trends for metal complexes with anticancer activity. *Curr. Opin. Chem. Biol.* **2008,** *12* (2), 197-206.

2. Frezza, M.; Hindo, S.; Chen, D.; Davenport, A.; Schmitt, S.; Tomco, D.; Dou, Q. P., Novel metals and metal complexes as platforms for cancer therapy. *Curr. Pharm. Des.* **2010,** *16* (16), 1813-25.

3. Ndagi, U.; Mhlongo, N.; Soliman, M. E., Metal complexes in cancer therapy – an update from drug design perspective. *Drug Design, Development and Therapy* **2017,** *11*, 599-616.

4. Kelland, L., The resurgence of platinum-based cancer chemotherapy. *Nat. Rev. Cancer* **2007,** *7* (8), 573-584.

5. Wheate, N. J.; Walker, S.; Craig, G. E.; Oun, R., The status of platinum anticancer drugs in the clinic and in clinical trials. *Dalton Trans.* **2010,** *39* (35), 8113-8127.

6. Farrell, N. P., Platinum Formulations as Anticancer Drugs Clinical and Pre-Clinical Studies. *Current Topics in Med. Chem.* **2011,** *11* (21), 2623-2631.

7. Stewart, D. J., Mechanisms of resistance to cisplatin and carboplatin. *Critical Reviews in Oncology Hematology* **2007,** *63* (1), 12-31.

8. Rabik, C. A.; Dolan, M. E., Molecular mechanisms of resistance and toxicity associated with platinating agents. *Cancer Treatment Reviews* **2007,** *33* (1), 9-23.

9. Lovejoy, K. S.; Lippard, S. J., Non-traditional platinum compounds for improved accumulation, oral bioavailability, and tumor targeting. *Dalton Trans.* **2009,** (48), 10651-10659.

10. Giandomenico, C. M.; Abrams, M. J.; Murrer, B. A.; Vollano, J. F.; Rheinheimer, M. I.; Wyer, S. B.; Bossard, G. E.; Higgins, J. D., Carboxylation of Kinetically Inert Platinum(IV) Hydroxy Complexes. An Entr.acte.ee into Orally Active Platinum(IV) Antitumor Agents. *Inorg. Chem.* **1995,** *34* (5), 1015-21.

11. Hall, M. D.; Mellor, H. R.; Callaghan, R.; Hambley, T. W., Basis for Design and Development of Platinum(IV) Anticancer Complexes. *J. Med. Chem.* **2007,** *50* (15), 3403-3411.

12. Johnstone, T. C.; Park, G. Y.; Lippard, S. J., Understanding and Improving Platinum Anticancer Drugs – Phenanthriplatin. *Anticancer Res.* **2014,** *34* (1), 471-476.

13. Wexselblatt, E.; Gibson, D., What do we know about the reduction of Pt(IV) pro-drugs? *J. Inorg. Biochem.* **2012,** *117*, 220-229.

14. Gibson, D., Multi-action Pt(IV) anticancer agents; do we understand how they work? *J. Inorg. Biochem.* **2019,** *191*, 77-84.

15. I. Riddell, S. J. L., V. Brabec, J. Kasparkova, V. Menon, N.P. Farrell, V. Venkatesh, P.J. Sadler, A.K. Gorle, E.J. Peterson, *Metallo-drugs: Development and Action of Anticancer Agents*. Walter de Gruyter GmbH & Co KG: **2018**.

16. Jia, C.; Deacon, G. B.; Zhang, Y.; Gao, C., Platinum(IV) antitumor complexes and their nano-drug delivery. *Coord. Chem. Rev.* **2021,** *429*, 213640.

17. Wilson, J. J.; Lippard, S. J., Acetate-Bridged Platinum(III) Complexes Derived from Cisplatin. *Inorganic Chemistry* **2012,** *51* (18), 9852-9864.

18. Stephen, E.; Blake, A. J.; Davies, E. S.; McMaster, J.; Schröder, M., The structural characterisation and elucidation of the electronic structure of the mononuclear Pt(iii) complex [Pt([9]aneS3)2]3+ ([9]aneS3 = 1,4,7-trithiacyclononane). *Chem. Commun.* **2008,** (44), 5707-5709.

19. Cervantes, G.; Marchal, S.; Prieto, M. J.; Perez, J. M.; Gonzalez, V. M.; Alonso, C.; Moreno, V., DNA interaction and antitumor activity of a Pt(III) derivative of 2-mercaptopyridine. *J Inorg Biochem* **1999,** *77* (3-4), 197-203.

20. Cervantes, G.; Prieto, M. J.; Moreno, V., Antitumour Activity of a pt(III) Derivative of 2-Mercaptopyrimidine. *Met Based Drugs* **1997,** *4* (1), 9-18.

21. Gencheva, G.; Tsekova, D.; Gochev, G.; Momekov, G.; Tyuliev, G.; Skumryev, V.; Karaivanova, M.; Bontchev, P. R., Synthesis, Structural Characterization, and Cytotoxic Activity of Novel Paramagnetic Platinum Hematoporphyrin IX Complexes: Potent Antitumor Agents. *Met Based Drugs* **2007,** *2007*, 67376.

22. González, V. c. M.; Fuertes, M. A.; Pérez-Alvarez, M. a. J.; Cervantes, G.; Moreno, V.; Alonso, C.; Pérez, J. M., Induction of apoptosis by the bis-Pt(III) complex [Pt2(2-mercaptopyrimidine)4Cl2]. *Biochemical Pharmacology* **2000,** *60* (3), 371-379.

23. Momekov, G.; Karaivanova, M.; Ugrinova, I.; Pasheva, E.; Gencheva, G.; Tsekova, D.; Arpadjan, S.; Bontchev, P. R., In vitro pharmacological study of monomeric platinum(III) hematoporphyrin IX complexes. *Investigational New Drugs* **2011,** *29* (5), 742-751.

24. Matsumoto, K.; Matsunami, J.; Mizuno, K.; Uemura, H., Organometallic Chemistry of an Amidate-Bridged Dinuclear Pt(III) Complex: Axial Pt(III)−Alkyl σ-Bond Formation in the Reaction with Acetone. *J. Am. Chem. Soc.* **1996,** *118* (37), 8959-8960.

25. Umakoshi, K.; Yamasaki, T.; Fukuoka, A.; Kawano, H.; Ichikawa, M.; Onishi, M., C−S Bond Cleavage of pyridine-2-thiol: A New Functionality of Quadruply Bridged Dinuclear Platinum and Palladium Complexes. *Inorg. Chem.* **2002,** *41* (16), 4093-4095.

26. Wu, X.; Chen, D.-G.; Liu, D.; Liu, S.-H.; Shen, S.-W.; Wu, C.-I.; Xie, G.; Zhou, J.; Huang, Z.-X.; Huang, C.-Y.; Su, S.-J.; Zhu, W.; Chou, P.-T., Highly Emissive Dinuclear Platinum(III) Complexes. *J. Am. Chem. Soc.* **2020,** *142* (16), 7469-7479.

27. Uemura, T.; Tomohiro, T.; Hayamizu, K.; Okuno, Y., Electron spin resonance of Pt(III) in anticancer platinum pyrimidine green. *Chem. Phys. Lett.* **1987,** *142* (5), 423-425.

28. Sicilia, V.; Borja, P.; Martín, A., Half-Lantern Pt(II) and Pt(III) Complexes. New Cyclometalated Platinum Derivatives. *Inorganics* **2014,** *2* (3).

29. Klein, A.; Hasenzahl, S.; Kaim, W.; Fiedler, J., On the Question of Mixed-Valent States in Ligand-Bridged Dinuclear Organoplatinum Compounds [RkPt(μ-L)PtRk]n, k = 2 or 4. *Organometallics* **1998,** *17* (16), 3532-3538.

30. Cini, R.; Fanizzi, F. P.; Intini, F. P.; Natile, G., SYNTHESIS AND X-RAY STRUCTURAL CHARACTERIZATION OF THE 1ST UNBRIDGED DIPLATINUM(III) COMPOUND - BIS BIS(1-IMINO-1-HYDROXY-2,2-DIMETHYLPROPANE)TRI-CHLOROPLATINUM(III). *Journal of the American Chemical Society* **1991,** *113* (20), 7805-7806.

31. Pellicani, R. Z.; Intini, F. P.; Maresca, L.; Mesto, E.; Pacifico, C.; Natile, G., The first example of a dinuclear platinum(III) complex with three bridging ligands. *Eur. J. Inorg. Chem.* **2006,** (8), 1635-1642.

32. Klein, A.; Kaim, W.; Hornung, F. M.; Fiedler, J.; Zalis, S., Electronic and molecular structure of 2,2'-bipyrimidine-bridged bis(organoplatinum) complexes in various oxidation states. Radical-bridged

diplatinum species and the absence of a Pt(III)/Pt(II) mixed-valent intermediate. *Inorg. Chim. Acta* **1997,** *264* (1), 269-278.

33. Rivada-Wheelaghan, O.; Ortuno, M. A.; Garcia-Garrido, S. E.; Diez, J.; Alonso, P. J.; Lledos, A.; Conejero, S., A stable, mononuclear, cationic Pt(III) complex stabilised by bulky N- heterocyclic carbenes. *Chem. Comm.* **2014,** *50* (11), 1299-1301.

34. Uson, R.; Fornies, J.; Tomas, M.; Menjon, B.; Sunkel, K.; Bau, R., The first mononuclear Pt complex. Molecular structures of $(NBu_4)[Pt(C_6Cl_5)_4]$ and of its parent compound $\{NBu_4\}_2[Pt(C_6Cl_5)_4].2CH_2Cl_2$. *J. Chem. Soc., Chem. Comm.* **1984,** (12), 751-752.

35. Stephen, E.; Blake, A. J.; Davies, E. S.; McMaster, J.; Schroder, M., The structural characterisation and elucidation of the electronic structure of the mononuclear Pt(iii) complex [Pt([9]aneS3)2]3+ ([9]aneS3 = 1,4,7-trithiacyclononane). *Chem. Commun.* **2008,** (44), 5707-5709.

36. Bélombé, M. M.; Nenwa, J.; Hey-Hawkins, E.; Lönnecke, P.; Strauch, P.; Koch, K. R., Synthesis, EPR spectrum and X-ray structure of tetra-n-butylammonium bis(benzene-1,2-dithiolato(2−)-κ2S,S')platinate(III). *Polyhedron* **2008,** *27* (18), 3688-3692.

37. Alonso, P. J.; Alcalá, R.; Usón, R.; Forniés, J., EPR study of mononuclear Pt(III) organometallic complexes. *J. Phys. Chem. Solids* **1991,** *52* (8), 975-978.

38. Hall, M. D.; Hambley, T. W., Platinum(IV) antitumour compounds: Their bioinorganic chemistry. *Coordination Chemistry Reviews* **2002,** *232* (1-2), 49-67.

39. Tolbatov, I.; Coletti, C.; Marrone, A.; Re, N., Insight into the Electrochemical Reduction Mechanism of Pt(IV) Anticancer Complexes. *Inorg. Chem.* **2018,** *57* (6), 3411-3419.

40. McCormick, M. C.; Keijzer, K.; Polavarapu, A.; Schultz, F. A.; Baik, M. H., Understanding Intrinsically Irreversible, Non-Nernstian, Two-Electron Redox Processes: A Combined Experimental and Computational Study of the Electrochemical Activation of Platinum(IV) Antitumor Prodrugs. *Journal of the American Chemical Society* **2014,** *136* (25), 8992-9000.

41. Klein, A.; Kaim, W., Axial Shielding of 5d8 and 5d7 Metal Centers in Dimesitylplatinum Complexes with Unsaturated Chelate Ligands: Spectroscopic and Spectroelectrochemical Studies of Four Different Oxidation States. *Organometallics* **1995,** *14* (3), 1176-1186.

42. Ojha, R.; Nafady, A.; Shiddiky, M. J. A.; Mason, D. N.; Boas, J. F.; Torriero, A. A. J.; Bond, A. M.; Deacon, G. B.; Junk, P. C., Conditions Favoring the Formation of Monomeric PtIII Derivatives in the Electrochemical Oxidation of trans-[PtII{(p-BrC6F4)NCH2CH2NEt2}Cl(py)]. *ChemElectroChem* **2015,** *2* (7), 1048-1061.

43. Ojha, R.; Boas, J. F.; Deacon, G. B.; Junk, P. C.; Bond, A. M., EPR spectroscopic characterization of a monomeric Pt^{III} species produced via electrochemical oxidation of the anticancer compound *trans*-$[Pt^{II}\{(p\text{-}HC_6F_4)NCH_2CH_2NEt_2\}Cl(py)]$. *J. Inorg. Biochem.* **2016,** *162*, 194-200.

44. Romero-Canelón, I.; Sadler, P. J., Next-Generation Metal Anticancer Complexes: Multitargeting via Redox Modulation. *Inorg. Chem.* **2013,** *52* (21), 12276-12291.

45. Jungwirth, U.; Kowol, C. R.; Keppler, B. K.; Hartinger, C. G.; Berger, W.; Heffeter, P., Anticancer activity of metal complexes: involvement of redox processes. *Antioxid. Redox Signal.* **2011,** *15* (4), 1085-1127.

46. Jungwirth, U.; Kowol, C. R.; Keppler, B. K.; Hartinger, C. G.; Berger, W.; Heffeter, P., Anticancer Activity of Metal Complexes: Involvement of Redox Processes. *Antioxid Redox Signal.* **2011,** *15* (4), 1085-1127.

47. Barry, H.; Veronique, C. M.; Hua, L. L., Hydrogen peroxide in the human body. *FEBS Letters* **2000,** *486* (1), 10-13.

48. Buxton, D. P.; Deacon, G. B.; Black, D., Organoamidometallics III. 2,6-Dimethylpyridine and 1,4-dioxan as weakly coordinating polar solvents for decarboxylation syntheses of N,N-dimethyl-N'-(polyfluorophenyl)ethane-1,2-diaminato(1-)platinum(II) complexes. *Polyhedron* **1989,** *8*, 143-147.

49. Buxton, D. P.; Deacon, G. B.; Gatehouse, B. M.; Grayson, I. L.; Black, D. S. C., Organoamidometallics. II. Decarboxylation Syntheses and Structures of [N,N-Dimethyl-N'-(Polyfluorophenyl)Ethane-1,2-Diaminato(1-)]Platinum(II) Complexes. *Aust. J. Chem.* **1988,** *41*, 943-956.

50. Deacon, G. B.; Gatehouse, B. M.; Ireland, J., ORGANOAMIDOMETALLICS .5. SYNTHESES OF N,N-DIETHYL-N'-POLYFLUOROPHENYL-ETHANE-1,2-DIAMINATO(1-) PLATINUM(II) COMPLEXES BY DECARBOXYLATION REACTIONS, AND THE X-RAY CRYSTAL-STRUCTURE OF TRANS-PT(NC6F5CH2CH2NET2)I(PY). *Aust. J. Chem.* **1991,** *44* (12), 1669-1681.

51. Battle, A. R.; Bond, A. M.; Chow, A.; Daniels, D. P.; Deacon, G. B.; Hambley, T. W.; Junk, P. C.; Mason, D. N.; Wang, J., Syntheses and structures of N-polyfluorophenyl- and N,N ' bis(polyfluorophenyl)ethane-1,2-diaminato(1-or 2-)platinum(II) complexes. *J. Fluorine Chem.* **2010,** *131* (11), 1229-1236.

52. Ojha, R.; Mason, D. N.; Forsyth, C. M.; Deacon, G. B.; Junk, P. C.; Bond, A. M., Diverse and unexpected outcomes from oxidation of the platinum(II) anticancer agent [Pt{(p-BrC6F4)NCH2CH2NEt2}Cl(py)] by hydrogen peroxide. *J. Inorg. Biochem.* **2021,** *218*, 111360.

53. Guo, S.-X.; Mason, D. N.; Turland, S. A.; Lawrenz, E. T.; Kelly, L. C.; Fallon, G. D.; Gatehouse, B. M.; Bond, A. M.; Deacon, G. B.; Battle, A. R.; Hambley, T. W.; Rainone, S.; Webster, L. K.; Cullinane, C., Systematic differences in electrochemical reduction of the structurally characterized anti-cancer platinum(IV) complexes [Pt{((p-HC6F4)NCH2)2}-(pyridine)2Cl2], [Pt{((p-HC6F4)NCH2)2}(pyridine)2(OH)2], and [Pt{((p-HC6F4)NCH2)2}(pyridine)2(OH)Cl]. *J. Inorg. Biochem.* **2012,** *115*, 226-239.

54. Frisch, M. J. T., G. W.; Schlegel, H. B.; Scuseria, G. E.; Robb, M. A.; Cheeseman, J. R.; Scalmani, G.; Barone, V.; Petersson, G. A.; Nakatsuji, H.; Li, X.; Caricato, M.; Marenich, A. V.; Bloino, J.; Janesko, B. G.; Gomperts, R.; Mennucci, B.; Hratchian, H. P.; Ortiz, J. V.; Izmaylov, A. F.; Sonnenberg, J. L.; Williams-Young, D.; Ding, F.; Lipparini, F.; Egidi, F.; Goings, J.; Peng, B.; Petrone, A.; Henderson, T.; Ranasinghe, D.; Zakrzewski, V. G.; Gao, J.; Rega, N.; Zheng, G.; Liang, W.; Hada, M.; Ehara, M.; Toyota, K.; Fukuda, R.; Hasegawa, J.; Ishida, M.; Nakajima, T.; Honda, Y.; Kitao, O.; Nakai, H.; Vreven, T.; Throssell, K.; Montgomery, J. A. Jr.; Peralta, J. E.; Ogliaro, F.; Bearpark, M. J.; Heyd, J. J.; Brothers, E. N.; Kudin, K. N.; Staroverov, V. N.; Keith, T. A.; Kobayashi, R.; Normand, J.; Raghavachari, K.; Rendell, A. P.; Burant, J. C.; Iyengar, S. S.; Tomasi, J.; Cossi, M.; Millam, J. M.; Klene, M.; Adamo, C.; Cammi, R.; Ochterski, J. W.; Martin, R. L.; Morokuma, K.; Farkas, O.; Foresman, J. B.; Fox, D. J., Gaussian 16, Revision B.01. *Gaussian, Inc., Wallingford CT* **2016**.

55. Lee, C.; Yang, W.; Parr, R. G., Development of the Colle-Salvetti correlation-energy formula into a functional of the electron density. *Phys. Rev. B: Condens. Matter* **1988,** *37* (2), 785-789.

56. Vosko, S. H.; Wilk, L.; Nusair, M., Accurate spin-dependent electron liquid correlation energies for local spin density calculations: a critical analysis. *Can. J. Phys.* **1980,** *58* (8), 1200-1211.

57. Becke, A. D., Density-functional thermochemistry. III. The role of exact exchange. *J. Chem. Phys.* **1993,** *98* (7), 5648-5652.

58. P. J. Stephens; F. J. Devlin; C. F. Chabalowski; Frisch, M. J., Ab Initio Calculation of Vibrational Absorption and Circular Dichroism Spectra Using Density Functional Force Fields. *J. Phys. Chem.* **1994,** *98* (45), 11623-11627.

59. Andrae, D.; Häußermann, U.; Dolg, M.; Stoll, H.; Preuß, H., Energy-adjustedab initio pseudopotentials for the second and third row transition elements. *Theor. Chim. Acta* **1990,** *77* (2), 123-141.

60. Andrae, H. H., U.; Dolg, M.; Stoll, H.; Preuss, H. , Energy-Adjustedab initio Pseudopotentials for the Second and Third Row Transition Element. *Theor. Chim. Acta* **1090,** *77*, 123-141.

61. NBO 6.0.Glendening, E. D. B., J. K.; Reed, A. E.; Carpenter, J. E.; Bohmann, J. A.; Morales, C. M.; Landis, C. R.; Weinhold, F. *NBO 6.0: Natural Bond Orbital Analysis program*, Theoretical Chemistry institute, University of Wisconsin, Madison, WI, **2013**.

62. Borg, S. J.; Best, S. P., Spectroelectrochemical cell for the study of interactions between redox-activated species and moderate pressures of gaseous substrates. *J. Electroanal. Chem.* **2002,** *535* (1–2), 57-64.

63. Best, S. P.; Borg, S. J.; Vincent, K. A., Ch. 1 Infrared Spectroelectrochemistry. In *Spectroelectrochemistry*, Kaim, W., Klein, A, Ed. The Royal Society of Chemistry: 2008; pp 1-30.

64. Best, S. P.; Levina, A.; Glover, C.; Johannessen, B.; Kappen, P.; Lay, P. A., XAS spectroelectrochemistry: reliable measurement of X-ray absorption spectra from redox manipulated solutions at room temperature. *J. Synchrotron Rad.* **2016,** *23* (3), 743-750.

65. Stoll, S.; Schweiger, A., EasySpin, a comprehensive software package for spectral simulation and analysis in EPR. *J. Magn. Reson.* **2006,** *178* (1), 42-55.

66. Bard, A. J., L. R. Faulkner, *Electrochemical Methods: Fundamentals and Applications*. second ed.; Wiley & Sons: New York 2001.

67. Johansson, L.; Ryan, O. B.; Rømming, C.; Tilset, M., Redox Chemistry of Dimethylplatinum(II) Diimine Complexes. Oxidatively Induced Pt−Me Transfer between Transient Platinum(III) Cation Radicals. *Organometallics* **1998,** *17* (18), 3957-3966.

68. Haputhanthi, R.; Ojha, R.; Izgorodina, E. I.; Guo, S.-X.; Deacon, G. B.; McNaughton, D.; Wood, B. R., A spectroscopic investigation into the binding of novel platinum(IV) and platium(II) anticancer drugs with DNA. *Vib. Spectrosc.* **2017,** *92*, 82-95.

69. Borg, S. J.; Tye, J. W.; Hall, M. B.; Best, S. P., Assignment of Molecular Structures to the Electrochemical Reduction Products of Diiron Compounds Related to [Fe−Fe] Hydrogenase: A Combined Experimental and Density Functional Theory Study. *Inorg. Chem.* **2007,** *46* (2), 384-394.

70. Cheah, M. H.; Best, S. P., XAFS and DFT Characterisation of Protonated Reduced Fe Hydrogenase Analogues and Their Implications for Electrocatalytic Proton Reduction. *Eur. J. Inorg. Chem.* **2011,** *2011* (7), 1128-1137.

71. Irmler, P.; Winter, R. F., σ-Pt-BODIPY Complexes with Platinum Attachment to Carbon Atoms C2 or C3: Spectroscopic, Structural, and (Spectro)Electrochemical Studies and Photocatalysis. *Organometallics* **2018,** *37* (2), 235-253.

72. Mason, D. N.; Deacon, G. B.; Yellowlees, L. J.; Bond, A. M., Electrochemical and chemical oxidation of the antitumour agent Pt{((p-HC6F4)NCH2)(2)}(py)(2) - detection of platinum(III) intermediates. *Dalton Trans.* **2003,** (5), 890-900.

73. Jiang, F.; Li, C.; Fu, H.; Guo, X.; Wu, G.; Chen, S., Probing the spontaneous reduction mechanism of platinum ions confined in the nanospace by X-ray absorption fine structure spectroscopy. *Phys. Chem. Chem. Phys.* **2016,** *18* (28), 19259-19266.

For Table of Contents Only

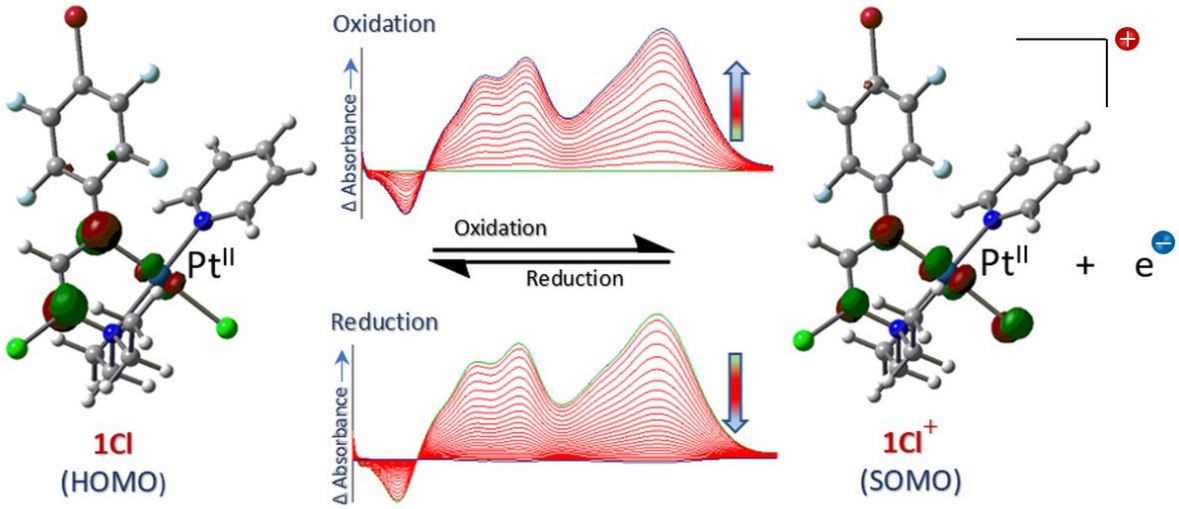

synopsis

Electrochemical, spectroscopic (visible, IR, EPR, XAS), and DFT studies provide insights into electron delocalization and bonding in the metalloradical $[Pt^{II}\{(p\text{-}BrC_6F_4)NCH{=}C(Cl)NEt_2\}Cl(py)]^+$, **1Cl**$^+$, complex obtained by electrochemical oxidation of $[Pt^{II}\{(p\text{-}BrC_6F_4)NCH{=}C(Cl)NEt_2\}Cl(py)]$, **1Cl**. The **1Cl/1Cl**$^+$ process displays chemical and electrochemical reversibility under short time scale voltammetric and long time scale bulk electrolysis conditions in CH_2Cl_2 . The stability of **1Cl**$^+$ is enhanced by greater delocalization of the unpaired electron onto the ligand system than found with related complexes.